Assessment and stenting of tracheal stenosis using deformable shape models

Rômulo Pinho [a,*], Kurt G. Tournoy [b], Jan Sijbers [a]

[a] IBBT-VisionLab, Department of Physics of the University of Antwerp, Belgium
[b] Department of Respiratory Medicine of the Ghent University Hospital, Belgium

ARTICLE INFO

ABSTRACT

This work presents a decision support system for the assessment of tracheal stenosis. In the proposed method, a statistical shape model of healthy tracheas is registered to a 3D CT image of a patient with tracheal stenosis. The registration yields an estimation of the shape of the patient's trachea as if stenosis was not present. From this point, the extent and the severity of the stenosis is assessed and stent parameters are obtained automatically. The method was extensively evaluated on simulation as well on real data and the results showed that it is accurate and fast enough to be used in the clinical setting.

© 2011 Elsevier B.V. All rights reserved.

1. Introduction

Tracheal stenosis is an unnatural narrowing of the trachea with traumatic, neoplastic, or idiopathic causes that, despite being relatively rare, can be life threatening (Spittle and McCluskey, 2000). Until now, tracheal resection surgery remains the preferred choice of treatment. In this modality, the narrowed part of the trachea is removed and the ends are sutured together (Elliott et al., 2003; Grillo et al., 1995).

When the stenosis is too long or when the patient status does not permit a surgical procedure, stent implants can render a successful solution to the stricture (Venuta et al., 2004; Saito and Imamura, 2005). Stents are tubular structures, currently made of silicone or metallic alloys, whose aim is to return normal breathing function to the patient by pushing the narrowed regions of the trachea. Since they are usually implanted with bronchoscopes, they reduce the surgical risk to the patient (Ching-Yang et al., 2007; Mandour et al., 2003; Miyazawa et al., 2004). Stents have also been used in tracheal reconstruction surgeries to aid the support and recovery of the reconstructed areas (Stamenkovic et al., 2007).

The choice of treatment is a direct result of the assessment of the stenosis. It means that, when assessing the strictures, it is important to correctly determine their location, length, and degree of severity (Boiselle et al., 2008). Traditionally, stenoses have been assessed with rigid or flexible bronchoscopy (Carretta et al., 2006; Nouraei et al., 2006). These methods, however, are invasive and require patient sedation. They also depend on the expertise of the specialist in charge and may not even serve their purpose if the stricture is too narrow to allow the passage of the bronchoscope itself.

With advances in the imaging field, image analysis has increasingly been used as a complementary tool for the assessment of stenosis, and CT is often the image modality of choice. A variety of methods have been proposed to assess stenosis using CT image analysis and processing. This includes evaluation of multi-slice CT scans and 3D reconstructions (Lee et al., 2005) and virtual bronchoscopy (Shitrit et al., 2005; Hoppe et al., 2004).

If a stent is to be used in the treatment, the assessment will also determine its dimensions and deployment location. Therefore, a pre-condition to a successful treatment is that the size and diameter of the tubes must be correctly estimated, otherwise problems such as stent migration and improper mucus clearance may occur (Venuta et al., 2004; Saito and Imamura, 2005; Prasad et al., 2002).

As an improvement to the traditional assessment methods, evaluations of the cross-sectional diameter of tracheas segmented from CT images have also been reported (Graham et al., 2000; Sorantin et al., 2002; Kiesler et al., 2007; Triglia et al., 2002; Valdes et al., 2000). In this approach, the profile of the tracheal diameter is plotted on a graph, which eases the visualization of the decrease in the diameter of the trachea and aids the operator in determining the start and end points of the stenosis. Nonetheless, neither of these or other traditional methods can easily indicate how much the stent should push the narrowed walls of the trachea, since they do not give a clear indication of the tracheal geometry if stenosis was not present.

Ballester et al. (2009) recently proposed a system for tracheal surgery planning and choice of stents from a pre-built stent database. Despite being a powerful visualization tool, the choice of

---

* Corresponding author. Address: University of Antwerp, Dept. Physics, Universiteitsplein 1, N.1.18, 2610 Antwerp, Belgium. Tel.: +32 3 2652474; fax: +32 3 2652245.

E-mail address: romulo.pinho@ua.ac.be (R. Pinho).

stent and its positioning in the image are done manually. To date, stenosis assessment and stent prediction remain very operator dependent operations.

Concomitantly with developments in the search for treatments for tracheal stenosis, active contour models (ACMs, or snakes; Kass et al., 1988) and active shape models (ASMs; Cootes et al., 1995) have been important tools in computer aided diagnoses. Both types of models are used to detect contours or other features in images. In addition, a distinctive characteristic of ASMs is that they only generate shapes that resemble those used in its training phase. de Bruijne et al. (2007) used this characteristic in pairwise conditional shape models trained on healthy spines to quantify vertebral fractures. In Rajamani et al. (2007), Zachow et al. (2005) the ASM was registered to manually selected points on the target surface, and the resulting shape was estimated from the statistical variation present in the ASM. In the case of the trachea, these methods tend not to be effective, because, firstly, there is no evident pairwise relationship to be modelled. Secondly, manually determining healthy areas on the 3D surface of the trachea can be impractical and prone to error.

With this in mind, the present work sets forth a decision support system for assessment of tracheal stenosis and prediction of stent dimensions using ASMs and ACMs applied to chest CT scans. The idea is to use an ASM of healthy tracheas to estimate the shape of a patient's trachea in case stenosis was not present. Fitting a healthy trachea shape model to a stenotic trachea is a challenge in itself. In other application domains, *Robust ASM Fitting* algorithms have been proposed to avoid the influence of non-target regions in the registration (Rogers and Graham, 2002; Behiels et al., 2002; de Bruijne et al., 2003; Theobald et al., 2006). Here, a new ASM registration method called *Fixed Landmarks* is proposed to avoid the influence of the narrowed regions of the target trachea on the registration.

This work further proposes to use an ACM to segment the narrowed trachea from the image, being initialized with the healthy trachea obtained with the ASM. The parameters of the stenosis (start, end, severity) and the patient-specific stent are then automatically computed from the two resulting tracheas.

An extensive set of simulation experiments was carried out in order to validate the proposed decision support system. The robustness of the *Fixed Landmarks* method is demonstrated through a comparison with a well-performing Robust ASM Fitting algorithm, as discussed in Pinho et al. (2009b), which employs weighted least squares minimization. Through a retrospective study with image data from nine patients, this work also demonstrates that the proposed method can overcome the typical operator dependency in the tracheal stenosis assessment and be used as a common ground to aid physicians in the their diagnostic processes.

2. Methods

In this section, all the methods developed for the proposed decision support system are presented. Section 2.1 describes how patients' healthy tracheas can be estimated from CT scans of their stenoses. Section 2.2 shows how these estimations are used in the assessment of the stenoses. Section 2.3 finally describes how patient-specific stents are chosen from the computed parameters of the stenoses.

2.1. Estimation of healthy tracheas

The motivation to use a statistical model of healthy tracheas to estimate the shape of a patient's trachea if stenosis was not present is that ASMs can only generate shapes that resemble those used in its training set. Since the model contains only instances of healthy tracheas, local geometric variations typical of stenosis cannot be generated. Nonetheless, when the model is registered to a narrowed trachea, the stricture can still influence the process, and globally narrowed tracheas may be generated. Next, the steps necessary for the construction of the model are shown in detail and a new method to avoid the influence of narrowed regions on the registration of the ASM to stenotic tracheas is proposed.

2.1.1. Training set

The statistical shape model is built from a training set of N shapes. Here, a set of surfaces of healthy tracheas segmented from CT images of the thorax is used. The region growing method presented in Pinho et al. (2009a) segments the trachea from the very beginning, below the vocal cords, down to the region of the carina, where the trachea splits into the two main bronchi. It also generates a good approximation of the centre line of the tracheas, which are used as the basis to achieve correspondence between the shapes of the training set.

Note that when selecting images for the training set, the method relies on the assumption that the CT scans include the complete trachea. If the scans start above the trachea, the region growing method mentioned above takes care of identifying its starting point. CT scans starting slightly below the point where the trachea starts, on the other hand, should not be used, since they will introduce errors in the construction of the statistical model.

2.1.2. Establishment of correspondences

To build an ASM, a one-to-one correspondence between the landmarks of the shapes in the training set is required. A direct result from the segmentations above is that the region below the vocal cords and the carina already correspond. The correspondence within the centre lines is achieved by arc-length parametrization. Each centre line is then smoothed with a cubic B-spline function and resampled, generating a set of points $\mathscr{C}_i, i = 1 \ldots N$ such that $|\mathscr{C}_i| = n_c, \ \forall i$.

The shapes of the training set, however, are described by points on their boundaries. The segmented trachea is thus sampled at constant angular intervals around each centre line point $\mathbf{c}_{ik}, k = 1 \ldots n_c$. The sampled points all lie on a plane perpendicular to the centre line. The generated contours are then smoothed with a cubic spline function, yielding curves $\mathscr{B}_{ik}$ with n_b points.

The correspondence may still be incorrect due to one remaining degree of freedom, which is the rotation of the tracheas around their centre lines. Supposing that all patients are scanned in the same position (prone or supine),[1] this degree can be removed by computing the orientation of the contour defining the region of the carina. This contour is elliptical and, once it is aligned with the axial plane, its major axis forms an angle α_c with the coronal direction. The boundary sampling procedure is thus modified in such a way that the first point of $\mathscr{B}_{ik}$ is always at an angle α_c w.r.t. the coronal direction.

Fig. 1 illustrates the whole concept. Each trachea is finally described by a smooth, triangular surface $\mathscr{S}_i = (\mathscr{X}_i, \mathscr{T}_i)$. The set of points, or landmarks, $\mathscr{X}_i$ results from the union of all $\mathscr{B}_{ik}$, such that $|\mathscr{X}_i| = n_c \times n_b = n$, and $\mathscr{T}_i$ is the set of triangles connecting the elements of $\mathscr{X}_i$.

2.1.3. Active shape model

After establishing the correspondences, each shape $\mathscr{S}_i$ has its set of landmarks $\mathscr{X}_i$ converted into a $3n$-dimensional vector $\mathbf{x}_i = (x_i = (x_{i11}, x_{i12}, x_{i13}, \ldots, x_{in1}, x_{in2}, x_{in3})^T$. The tracheas are then aligned w.r.t. location and pose and normalized w.r.t. scale, such that

---

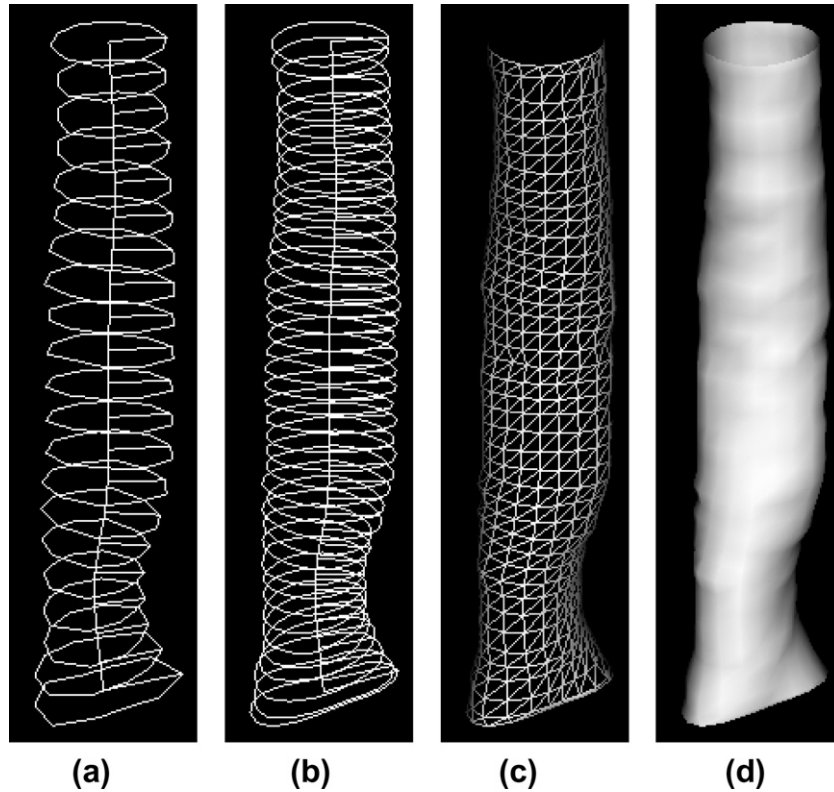[1] The image can always be flipped if this supposition fails.

Fig. 1. Transforming the shapes of the training set from a centre line to a boundary representation and establishing correspondences between them. (a) Centre line after arc-length parametrization. (b) Smoothed centre line $\mathscr{C}_i$ and respective contours $\mathscr{B}_{ik}$. (c) Smooth surface $\mathscr{S}_i$, in wireframe mode. (d) Smooth surface $\mathscr{S}_i$, in shaded mode. The lines crossing the contours of (a–c) indicate the position at which the sampling of the boundary starts (the region of the carina corresponds to the bottom contour).

$|\mathbf{x}_i| = 1$. Principal Component Analysis (PCA) extracts the eigenvectors, $\mathbf{p}_i$, and eigenvalues, λ_i, of the covariance matrix of all $\mathbf{x}_i$'s. The eigenvectors, also referred to as the main modes of variation of the training set, are grouped in an orthonormal matrix $\mathbf{P}_{3n \times N}$. New healthy tracheas can be obtained with this model, called a point distribution model (PDM), by linearly combining the mean shape with a weighted version of the eigenvector matrix $\mathbf{P}$, that is

$$\mathbf{x} = \bar{\mathbf{x}} + \mathbf{Pb}. \tag{1}$$

The vector $\mathbf{b} = (b_1, b_2, \ldots, b_N)^T$ is the set of parameters of the model and represents the contribution of each eigenvector. Since λ_i represents the variance of the training set along the eigenvector $\mathbf{p}_i$, the range $[-3\sqrt{\lambda_i}, +3\sqrt{\lambda_i}]$ is a suitable limit for b_i (Cootes et al., 1995).

2.1.4. ASM registration

ASMs can be registered to an object of the class they represent by adjusting $\mathbf{b}$. When the model is applied to an image, the registration is usually an iterative, edge based search. It encompasses an initialization step, followed by rigid and non-rigid registration stages. In the latter two, the landmarks of the shape generated by the model, $\mathbf{x}$, are moved along their normals towards high gradients corresponding to edges of the target, generating a candidate shape $\mathbf{y}$. Depending on the stage, either just pose or pose and shape are changed so as to let the model fit to $\mathbf{y}$. The registration is described in detail in the following.

2.1.4.1. Initialization. Since the registration is an edge based search, it can be misled by neighbouring organs and structures as well as noise. Therefore, the registration is dependent on the initial search location. The initialization can be done automatically, but this is a problem on its own and as such is out of the scope of this work. At this point, the initialization of the registration is done manually,

and the operator is given controls to change the position, scale, and orientation of the average shape of the model. The procedure should take in the order of seconds, so that the average shape can be quickly and conveniently placed in the image, namely, near the target trachea.

2.1.4.2. Rigid alignment. The registration of the ASM is divided into two stages. In the first step, the average shape of the model is rigidly aligned with the candidate shape $\mathbf{y}$ of each iteration. The search for high gradients is done at discrete steps within long profiles along the normals of the average shape. The rigid alignment stops when no significant change is made to the average shape at consecutive iterations or when a maximum number of iterations is reached. The purpose of this step is to find the best position and orientation of the average shape w.r.t. the target shape.

2.1.4.3. Pose and shape registration. In the second stage of the ASM registration, a non-rigid registration, which optimizes pose and shape, is started, and the landmarks of the shape generated by the model at the current iteration are again displaced along their normals. Once the candidate shape $\mathbf{y}$ is projected into model space, which aligns $\mathbf{y}$ with the average shape, a new set $\hat{\mathbf{b}}$ that defines the best fit of the model to $\mathbf{y}$ is obtained by minimization of the squared error between $\mathbf{y}$ and $\mathbf{x}$, resulting in

$$\hat{\mathbf{b}} = \mathbf{P}^T(\mathbf{y} - \bar{\mathbf{x}}). \tag{2}$$

This minimization is herein referred to as *StandardLS*. A new shape $\hat{\mathbf{x}}$ is generated from $\hat{\mathbf{b}}$, using Eq. (1), and is transformed back into the image space. The displacement of landmarks and the update of $\mathbf{b}$ and $\hat{\mathbf{x}}$ are repeated until no significant changes are made to $\hat{\mathbf{x}}$ (Cootes et al., 1995).

2.1.4.4. Fixed landmarks. Although the registration of the model of healthy tracheas to a trachea with stenosis tends not to be affected by the local geometric variations of the stricture, the registration may still produce globally narrowed tracheas. The proposed *Fixed Landmarks* overcomes this problem by setting a restriction on the displacement of landmarks, which defines the candidate shape **y**. Namely, if the candidate locations are not within a short threshold distance $d > 0$ from **x**, the corresponding landmarks of **y** remain fixed, while the other landmarks are allowed to move as usual.

Let $\mathbf{x}_{\mathbf{v}_j} = (x_{j1}, x_{j2}, x_{j3})^T$ be a landmark in a 3n-dimensional shape vector $\mathbf{x} = (x_{11}, x_{12}, x_{13}, \ldots, x_{n1}, x_{n2}, x_{n3})^T$. Let $\hat{\mathbf{x}}^{(k)} = \bar{\mathbf{x}} + \mathbf{P}\hat{\mathbf{b}}^{(k)}$ be the shape generated by the model at iteration k of the non-rigid registration. Let $\mathbf{y}^{(k+1)}$ be the candidate shape generated by displacing the landmarks of $\hat{\mathbf{x}}^{(k)}$, assuming that $\mathbf{y}^{(k+1)}$ has already been projected into model space and aligned with $\bar{\mathbf{x}}$.

Let now $d\mathbf{y}_{\mathbf{v}_j}^{(k+1)} = \mathbf{y}_{\mathbf{v}_j}^{(k+1)} - \hat{\mathbf{x}}_{\mathbf{v}_j}^{(k)}$, if $|\mathbf{y}_{\mathbf{v}_j}^{(k+1)} - \hat{\mathbf{x}}_{\mathbf{v}_j}^{(k)}| \leqslant d$, and $d\mathbf{y}_{\mathbf{v}_j}^{(k+1)} = \mathbf{0}$ otherwise, with $d\mathbf{y}^{(k+1)}$ the concatenation of all $d\mathbf{y}_{\mathbf{v}_j}^{(k+1)}$.

Using the definitions above, Eq. (2) can be rewritten as:

$$\hat{\mathbf{b}}^{(k+1)} = \mathbf{P}^T(\hat{\mathbf{x}}^{(k)} + d\mathbf{y}^{(k+1)} - \bar{\mathbf{x}}). \tag{3}$$

Let us now group the $d\mathbf{y}_{\mathbf{v}_j}^{(k+1)} = \mathbf{0}$ and the corresponding rows of $\hat{\mathbf{x}}^{(k+1)}$ and $\bar{\mathbf{x}}$, and columns of $\mathbf{P}^T$, using row and column permutations, respectively. This results in two subsets of landmarks, $\mathscr{L}'$ and $\mathscr{L}''$, of sizes n' and n'', respectively, such that $d\mathbf{y}^{(k+1)}|_{\mathscr{L}''} = \mathbf{0}$. Eq. (3) can then be split into

$$\hat{\mathbf{b}}^{(k+1)} = \left[\mathbf{P}^T(\hat{\mathbf{x}}^{(k)} + d\mathbf{y}^{(k+1)} - \bar{\mathbf{x}})\right]\Big|_{\mathscr{L}'}$$
$$+ \left[\mathbf{P}^T(\hat{\mathbf{x}}^{(k)} + d\mathbf{y}^{(k+1)} - \bar{\mathbf{x}})\right]\Big|_{\mathscr{L}''}, \tag{4}$$

which does not affect the result. Since $d\mathbf{y}^{(k+1)}|_{\mathscr{L}''} = \mathbf{0}$, the parameters are finally given by

$$\hat{\mathbf{b}}^{(k+1)} = \left[\mathbf{P}^T(\mathbf{y}^{(k+1)} - \bar{\mathbf{x}})\right]\Big|_{\mathscr{L}'} + \left[\mathbf{P}^T(\hat{\mathbf{x}}^{(k)} - \bar{\mathbf{x}})\right]\Big|_{\mathscr{L}''}. \tag{5}$$

Eq. (5) shows that $\hat{\mathbf{b}}^{(k+1)}$ is determined by both the displaced landmarks $\mathbf{y}^{(k+1)}|_{\mathscr{L}'}$ and the landmarks $\hat{\mathbf{x}}^{(k)}|_{\mathscr{L}''}$, which remained fixed.[2] Consequently, when computing

$$\hat{\mathbf{x}}^{(k+1)} = \bar{\mathbf{x}} + \mathbf{P}\hat{\mathbf{b}}^{(k+1)}, \tag{6}$$

$\hat{\mathbf{x}}^{(k+1)}$ will be the best fit, in a least squares minimization sense, to $\mathbf{y}^{(k+1)}|_{\mathscr{L}'}$ and $\hat{\mathbf{x}}^{(k)}|_{\mathscr{L}''}$. Provided that there are enough healthy areas around regions with stenosis, the fixed landmarks force the shape generated by the model to remain far from those regions, while enabling correct matches at the healthy areas. As the shape deforms iteratively, it progressively assumes the form of the desired healthy trachea, guided by the regions where correct matches occur. Setting $d = 1$ mm proved to be a good empirical choice in experiments with simulation and clinical data.

2.2. Assessment of tracheal stenosis

The healthy trachea estimated above is the basis for the automatic assessment of stenosis. This assessment is performed via a comparison between the cross-sectional area profiles of the estimated healthy trachea and the narrowed trachea in the image. It is thus necessary to segment the narrowed trachea in question from the given CT image, which is done with an active contour model tailored for this purpose. The steps involved in this segmentation and in the quantification of the stenosis are presented in the following.

2.2.1. Active contour models

ACMs, commonly known as Snakes, are curves defined within an image domain that are able to move under the influence of internal forces derived from the curve itself and of external forces derived from the image data. While moving, the curve will register to an object boundary or other desired features within an image. As defined by Kass et al. (1988), a snake can be represented in 2D by a curve $\mathbf{v}(s) = (x(s), y(s))$, $s \in [0, 1]$, responding to an energy functional of the form:

$$E = \int_0^1 [\kappa E_{int}(\mathbf{v}(s)) + (1 - \kappa)E_{ext}(\mathbf{v}(s))]ds, \tag{7}$$

where $\kappa \in [0, 1]$ is a weighting factor. The internal energy E_{int} restricts the deformations taking into account curvature and elasticity. The external energy causes the curve to be attracted by high image gradients.

The objective is then to minimize Eq. (7), making the system a force balance equation of the form:

$$\kappa \mathbf{F_{int}} + (1 - \kappa)\mathbf{F_{ext}} = \mathbf{0}, \tag{8}$$

where

$$\mathbf{F_{int}} = -\nabla E_{int} \tag{9}$$

and

$$\mathbf{F_{ext}} = -\nabla E_{ext}. \tag{10}$$

The minimization is solved iteratively. The expected result is a curve that matches the high gradients of the image while being restricted by the internal constraints, according to the assigned weighting factors.

2.2.2. Segmentation of the stenotic trachea

The ACM above naturally extrapolates to 3D and can easily be adapted to a discrete domain. Within the context of the proposed application, a discrete surface can be defined as $\mathscr{S} = (\mathscr{X}, \mathscr{T})$, where $\mathscr{X}$ is the set of landmarks and $\mathscr{T}$ is the set of triangles connecting the points of $\mathscr{X}$ ($\mathscr{X}$ preserves the shape vector structure defined in Section 2.1.3). The internal and external forces are defined locally, and the minimization iterates through all the points of the surface. The process stops when no significant deformation is applied to the surface. Next, the integration of the ACM into the proposed method is explained.

2.2.2.1. Initialization. A classical problem with ACMs is initialization. The starting curve should be placed near the features of interest, otherwise the capture range of the external energy may not extend enough to attract the curve.

The ACM in this work is initialized with the estimated healthy shape obtained with the ASM above. Consequently, this shape is already close enough to the healthy regions of the trachea. It is also expected that the parts of the healthy shape corresponding to the narrowed regions of the trachea in the image will be in the capture range of the external force generated from those regions. Then, those parts of the healthy shape shrink under the influence of the external force until they match the walls of the narrowed trachea.

2.2.2.2. External force. The external energy of the ACM is commonly derived from the gradient of an image I convolved with a Gaussian function G at scale σ. In this work, the ideas presented in Cohen and Cohen (1993) are adapted so as to create an external force to guide the deformation of the surface. First, the original image, I, is thresholded to segment air and the result is then inverted. This generates two binary images, I_{B1} and I_{B2}. Afterwards, a 3-4-5 chamfer distance transform (Borgefors, 1986) is applied to each binary image, yielding two distance maps, I_{D1} and I_{D2}, respectively. In

---

[2] Note that $\mathscr{L}'$ and $\mathscr{L}''$ can be different at each iteration.

the last step, both distance transforms are combined into a new distance map $I_D = I_{D1} + I_{D2}$.

Eventually, the external force term of Eq. (8) applied to the landmark $\mathbf{x}_{\mathbf{v}_j}$ of $\mathscr{S}$ is defined as

$$\mathbf{F}_{\mathbf{ext}_j} = -\frac{|\nabla I_D(\mathbf{x}_{\mathbf{v}_j})|}{M}\nabla I_D(\mathbf{x}_{\mathbf{v}_j}), \qquad (11)$$

where M is the maximum gradient magnitude in I_D.

2.2.2.3. Internal forces. The internal forces of the ACM control stretching and bending. Considering stretching, or elasticity, the model prevents the curve from breaking apart, maintaining its continuity. As for bending, or curvature, the internal energy avoids the appearance of sharp corners.

The internal elastic force tries to keep the landmarks of $\mathscr{S}$ equally spaced by moving them towards a central point relative to their neighbours. This force is defined as

$$\mathbf{F}_{\mathbf{elast}_j} = D_j\frac{\mathbf{d}_{\mathbf{elast}_j}}{|\mathbf{d}_{\mathbf{elast}_j}|}. \qquad (12)$$

The directional component $\mathbf{d}_{\mathbf{elast}_j}$ is given by

$$\mathbf{d}_{\mathbf{elast}_j} = \mathbf{c}_{\mathbf{elast}_j} - \mathbf{x}_{\mathbf{v}_j}, \qquad (13)$$

where $\mathbf{c}_{\mathbf{elast}_j}$ is a point at a central location relative to the neighbours of $\mathbf{x}_{\mathbf{v}_j}$, such that:

$$\mathbf{c}_{\mathbf{elast}_j} = \begin{cases} \delta_j(\mathbf{x}_{\mathbf{v}_j} + \mathbf{n}_j), & \text{if } \mathbf{x}_{\mathbf{v}_j} \text{ is a border point} \\ \frac{1}{|\mathscr{O}_r(\mathbf{x}_{\mathbf{v}_j})|}\sum_{\mathbf{p}\in\mathscr{O}_r(\mathbf{x}_{\mathbf{v}_j})}\mathbf{p}, & \text{otherwise} \end{cases}, \qquad (14)$$

In the above, δ_j is the shortest distance from $\mathbf{x}_{\mathbf{v}_j}$ to the bisector plane of the imaginary line connecting its two immediate border[3] neighbours. This plane is specified by the normal vector $\mathbf{n}_j$. $\mathscr{O}_r$, in turn, is the ordered set of points directly connected to $\mathbf{x}_{\mathbf{v}_j}$, namely, its One-ring.

The scalar component, D_j, of $\mathbf{F}_{\mathbf{elast}_j}$ is a normalized measure of how much $\mathbf{x}_{\mathbf{v}_j}$ deviates from $\mathbf{c}_{\mathbf{elast}_j}$:

$$D_j = \left(1 - \frac{\sum_{\mathbf{p}\in\mathscr{N}(\mathbf{x}_{\mathbf{v}_j})}|\mathbf{p} - \mathbf{c}_{\mathbf{elast}_j}|}{\sum_{\mathbf{p}\in\mathscr{N}(\mathbf{x}_{\mathbf{v}_j})}|\mathbf{p} - \mathbf{x}_{\mathbf{v}_j}|}\right). \qquad (15)$$

In Eq. (15), $\mathscr{N}$ contains the two immediate border neighbours of $\mathbf{x}_{\mathbf{v}_j}$ if $\mathbf{x}_{\mathbf{v}_j}$ is a border point, or $\mathscr{N} = \mathscr{O}_r$ otherwise.

The internal bending force tries to move the points of the surface in such a way that they are all coplanar. This force is defined as

$$\mathbf{F}_{\mathbf{bend}_j} = K_{G_j}\frac{\mathbf{d}_{\mathbf{bend}_j}}{|\mathbf{d}_{\mathbf{bend}_j}|}. \qquad (16)$$

Its directional component, $\mathbf{d}_{\mathbf{bend}_j}$, also varies according to the location of point $\mathbf{x}_{\mathbf{v}_j}$, that is:

$$\mathbf{d}_{\mathbf{bend}_j} = \begin{cases} \mathbf{d}_{\mathbf{elast}_j}, & \text{if } \mathbf{x}_{\mathbf{v}_j} \text{ is a border point or } \mathbf{d}_{\mathbf{elast}_j} \perp \mathbf{n}_{\mathbf{v}_j} \\ sign(\langle\mathbf{d}_{\mathbf{elast}_j}, \mathbf{n}_{\mathbf{v}_j}\rangle)\mathbf{n}_{\mathbf{v}_j}, & \text{otherwise} \end{cases}, \qquad (17)$$

where $\mathbf{n}_{\mathbf{v}_j}$ is the normal of $\mathscr{S}$ at point $\mathbf{x}_{\mathbf{v}_j}$. This means that $\mathbf{F}_{\mathbf{bend}_j}$ will either move $\mathbf{x}_{\mathbf{v}_j}$ as $\mathbf{F}_{\mathbf{elast}_j}$ does or it will move the point along its normal.

The scalar component, K_{G_j}, of $\mathbf{F}_{\mathbf{bend}_j}$ is taken from the normalized, discrete Gaussian curvature of $\mathscr{S}$ at $\mathbf{x}_{\mathbf{v}_j}$ and is given by

$$K_{G_j} = \left(1 - \frac{1}{2\pi}\sum_{\mathbf{p}_1,\mathbf{p}_2\in\mathscr{N}(\mathbf{x}_{\mathbf{v}_j})}\angle\mathbf{x}_{\mathbf{v}_j}\mathbf{p}_1\mathbf{p}_2\right). \qquad (18)$$

---

[3] Border points are located at the surface's open ends.

In Eq. (18), $\mathscr{N}$ is defined as in Eq. (15) and $\angle\mathbf{x}_{\mathbf{v}_j}\mathbf{p}_1\mathbf{p}_2$ determines the angle between edges connecting two consecutive points of $\mathscr{N}$ with $\mathbf{x}_{\mathbf{v}_j}$.

Finally, the internal force term of Eq. (8) at landmark $\mathbf{x}_{\mathbf{v}_j}$ of $\mathscr{S}$ is defined as

$$\mathbf{F}_{\mathbf{int}_j} = \gamma\mathbf{F}_{\mathbf{elast}_j} + (1 - \gamma)\mathbf{F}_{\mathbf{bend}_j}, \qquad (19)$$

and for each iteration k of the deformation algorithm of the ACM,

$$\mathbf{x}_{\mathbf{v}_j}^{(k)} = \mathbf{x}_{\mathbf{v}_j}^{(k-1)} + \kappa\mathbf{F}_{\mathbf{int}_j} + (1 - \kappa)\mathbf{F}_{\mathbf{ext}_j}. \qquad (20)$$

2.2.3. Quantification of stenosis

Once healthy and narrowed tracheas are obtained, the assessment of the stenosis is straightforward. Let $\mathscr{S}_h = (\mathscr{X}_h, \mathscr{T}_h)$ be the triangular surface corresponding to the estimated healthy trachea and $\mathscr{S}_s = (\mathscr{X}_s, \mathscr{T}_s)$ the surface corresponding to the trachea with stenosis. Since $\mathscr{S}_h$ preserves the $|\mathscr{X}_h| = n_c \times n_b = n$ structure defined in Section 2.1.1, its centre line can easily be obtained as the n_c centres of gravity of the contours $\mathscr{B}_{hk}$ with n_b points. Let $\mathscr{A}_h$ be the area profile of $\mathscr{S}_h$, computed as the areas of the contours $\mathscr{B}_{hk}$.

The surface $\mathscr{S}_s$ is intersected with the planes containing the contours $\mathscr{B}_{hk}$, generating a set of contours $\mathscr{B}_{sk}$. In this way, both the healthy and narrowed versions of the trachea are now represented by a set of contours perpendicular to their centre lines. Let now $\mathscr{A}_s$ be the area profile of $\mathscr{S}_s$, analogously to $\mathscr{S}_h$. $\mathscr{A}_s$ will show a decrease in area at some points, and a comparison between $\mathscr{A}_h$ and $\mathscr{A}_s$ determines the point where the stenosis starts, its length, and the degree of narrowing. Algorithm 1 details this procedure.

The algorithm receives as input the set of contours of the estimated healthy trachea, $\mathscr{B}_h$, along with its area profile, $\mathscr{A}_h$, and the area profile of the contours of the stenotic trachea, $\mathscr{A}_s$.

Let $\mathscr{S}_T$ be a section of the estimated healthy trachea corresponding to the subset of $\mathscr{B}_h$ that covers the region with stenosis. The process starts with the initialization of $\mathscr{S}_T$ and of a temporary variable, $\mathscr{S}_0$, which, as $\mathscr{S}_T$, is a set of contours. Next, for all contours of the estimated healthy trachea, if the ratio between the areas of healthy and stenotic surfaces is below a given threshold, R_0, $\mathscr{S}_0$ is incremented with the corresponding contour from $\mathscr{B}_h$. If not, and if the length of $\mathscr{S}_0$ is below another given threshold, L_0, the temporary variable is emptied, as shown in Step 6. This test avoids the inclusion of very short segments in the set. If $\mathscr{S}_0$ is long enough, it is finally added to $\mathscr{S}_T$, in Step 8. In the end, the algorithm returns as a result the contours contained in $\mathscr{S}_T$.

Algorithm 1. predict_stent($\mathscr{B}_h, \mathscr{A}_h, \mathscr{A}_s$)

```
1:  𝒮_T ← ∅, 𝒮_0 ← ∅
2:  for k = 1 to |ℬ_h|
3:      if (A_sk/A_hk < R_0)
4:          𝒮_0 ← 𝒮_0 + ℬ_hk
5:      els if (length(𝒮_T) ⩽ L_0)
6:          𝒮_0 ← ∅
7:      else
8:          𝒮_T ← 𝒮_T + 𝒮_0
9:          𝒮_0 ← ∅
10:     end if
11: end for
12: return 𝒮
```

From $\mathscr{S}_T$, the parameters of the stenosis are calculated as follows:

1. *start point:* taken as the centre point of the contour $\mathscr{B}_{sk}$ that precedes the first contour of $\mathscr{S}_T$;
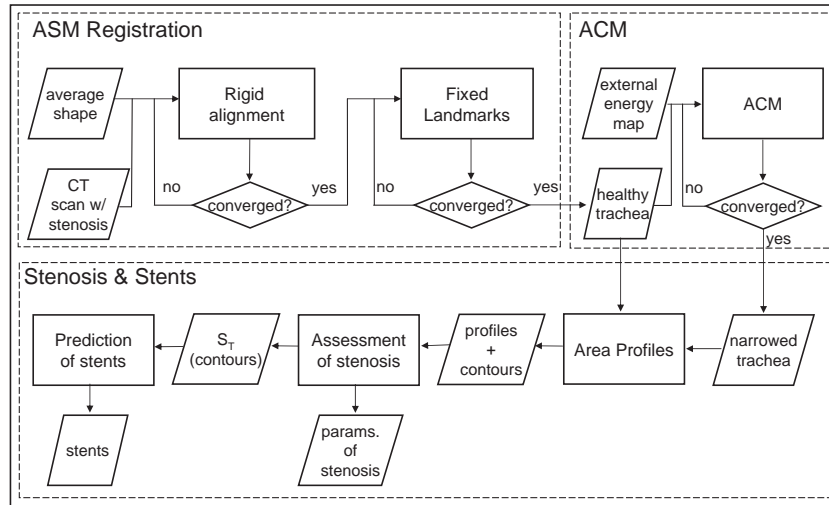
Fig. 2. Flowchart of the proposed method.

2. *end point:* taken as the centre point of the contour $\mathcal{B}_{sk}$ that succeeds the last contour of $\mathcal{S}_T$;

3. *degree of narrowing:* taken as the smallest ratio computed between the area profiles of $\mathcal{B}_h$ and $\mathcal{B}_s$.

2.3. Prediction of stents

The stent parameters can also be obtained from set $\mathcal{S}_T$ returned by Algorithm 1. The calibre of the stent is the average diameter of all contours in $\mathcal{S}_T$. The deployment location is equal to the start point of the stenosis. Finally, the length of the stent is the path length between the start and end points.

By adjusting the thresholds R_0 for the severity and L_0 for the extent of the stenosis, the number and dimensions of the predicted stents can be further adjusted. The applied changes can immediately be evaluated through a visual interaction between the operator and the application, which aids in deciding if the stent is the ideal treatment and in the surgery planning in general.

At this point, all the necessary steps for the assessment and stenting of tracheal stenosis using ASMs and ACMs have been described. Fig. 2 shows a flowchart which illustrates the proposed method. The next section presents the experiments employed in its validation.

3. Experiments

Experiments on simulation as well as on clinical data were carried out in order to evaluate the proposed method. With the simulation data, ground truths of measurements of stenoses were formally established in order to quantitatively evaluate the method. The experiments with clinical data were used for objective and subjective evaluations.

To build the ASM, $N = 38$ healthy tracheas were used, each with $n = 820$ landmarks. The chest CT scans of their respective patients were obtained from pulmonary medication studies carried out at the University Hospital of Antwerp, Belgium, and from the Lung Image Database Consortium (LIDC). Patient data were anonymized before the images were used. The tracheas were segmented from the images and converted to 3D surfaces with the procedure described in Section 2.1.1 before the model was built.

3.1. Simulation data

The proposed method was quantitatively evaluated with a large set of leave-one-out tests using simulation data. First, for a subset

of $N' = 10$ tracheas randomly taken from the training set, 72 phantoms of stenosis – 24 anteriorly (A), 24 posteriorly (P), and 24 roughly symmetrically narrowed (S) – were created from each element. The stenotic areas were generated by applying a local erosion mask to the binary images of the segmented healthy tracheas until the stenosis achieved the desired shape. The phantoms followed the categories of Tables 1 and 2, based on Freitag et al. (2007), and were validated by an expert in the pulmonology field. For example, phantom 5.I-1P represents a posterior stenosis of less than 25% along the upper third of trachea number 5.

For each run of the $T = N'$ leave-one-out tests, the model was built with $N - 1$ tracheas and was then registered to the 72 phantoms created from the healthy trachea not present in the training set. The quality of the assessment of stenosis and prediction of stents using the ASM strongly depends on the estimation of the healthy trachea of the patient. Therefore, the objective of this set of experiments was twofold. First, the aim was to quantify the quality of the estimation of the healthy trachea alone. To this end, the ASM was registered to the phantoms of stenosis (720 in total) using the *Fixed Landmarks* method and the error between the estimated healthy tracheas and their originally healthy counterparts was measured. The error was computed as the Hausdorff distance between the two surfaces, using the algorithm proposed by Aspert et al. (2002). The second objective was to measure the quality of the automatic assessment of the stenosis. From the estimated healthy tracheas, the stenotic phantoms were segmented using the ACM proposed in Section 2.2.2 and the stenoses were quantified using the healthy and narrowed versions of the tracheas, as described in Section 2.2.3. The results obtained for the parameters of the stenosis were then compared to the ground truth parameters. The latter were in turn computed in the same way, but using the originally healthy tracheas as the reference, instead of the estimated ones.

The same set of experiments was run with another ASM registration method to estimate the healthy shape of the patient's trachea. This method is based on weighted least squares minimization using the Talwar function to assign weights as a function of the landmark displacements during the registration. Such method is herein referred to as *TalwarWLS*. The purpose of running these experiments was to confirm that in order to achieve good results in the assessment of the stenoses, an ASM registration method that avoids the narrowed regions of target trachea must be employed. For details on the *TalwarWLS* and other Robust ASM Fitting methods used in the estimation of healthy tracheas, please see (Pinho et al., 2009b).

Table 1
Categories of stenosis based on location and length.

Category	Location and length
I	Upper third of the trachea
II	Middle third of the trachea
III	Lower third of the trachea
I–II	Upper third extending to middle third
II–III	Middle third extending to lower third
I–III	Upper third extending to lower third

Table 2
Categories of stenosis based on its degree of narrowing.

Category	Degree (%)
1	<25
2	26–50
3	51–75
4	>75

The iteration limit for the registration of the ASM was set to 200, high enough to enable the registrations to find a resting point, in which few surface changes would be observed between iterations. The minimum squared error between shapes generated at consecutive iterations, i.e., $\xi_r^{(k)} = (\mathbf{x}^{(k)} - \mathbf{x}^{(k-1)})^T (\mathbf{x}^{(k)} - \mathbf{x}^{(k-1)})$, was set to 10^{-5} mm^2. This parameter is somewhat coupled with the number of iterations and was small enough to interrupt the registration when there was no significant change in the shapes of consecutive iterations. Regarding the *Fixed Landmarks*, the landmarks were only displaced if the corresponding high gradients were found within a distance $d = 1$ mm along their normals.

For the ACM, the values used as weights for the forces where $\kappa = 0.7$ and $\gamma = 0.5$. These are traditionally difficult parameters to define and usually depend on the quality of the image and on the application itself. Here, the purpose was to give some freedom to the external force, since the local deformations of the stenoses needed to be correctly modelled. The iteration limit was set to 200 and $\xi_r^{(k)} = 10^{-3}$ mm^2.

Finally, for the quantification of the stenosis, Algorithm 1 used $R_0 = 0.8$, which balances the false positive and detection rates of the start, end, and narrowest points of the stenoses. The threshold L_0 was equivalent to the distance covered by two consecutive centre line points.

3.2. Clinical data

In addition to the simulation experiments, a retrospective study with 11 CT scans, from nine patients, was executed. The use of the CT scans was approved by the ethics committee of the Ghent University Hospital (doc. ECUZG2009/140), Belgium, and patient data were anonymized before the images were used in the experiments. The patients had stenosis with the following characteristics:

Patient 1 – Severe symmetrical stenosis along the upper third of the trachea.

Patient 2 – Side-to-side stenosis along the lower two thirds of the trachea.
Patient 3 – Severe symmetrical stenosis along the lower two thirds of the trachea.
Patient 4 – Severe posterior stenosis along the lower two thirds of the trachea (2 scans).
Patient 5 – Suspected, short anterior stenosis at the lower half of the trachea.
Patient 6 – Severe long segment posterior stenosis.
Patient 7 – Severe posterior stenosis along the upper two thirds of the trachea.
Patient 8 – Short anterior stenosis above the carina (2 scans).
Patient 9 – Symmetrical stenosis along the upper third of the trachea.

For the registration of the ASM, no preprocessing was applied to the CT images, even though some of them were very anisotropic in the axial direction. The original images were converted to a distance map through the steps described in Section 2.2.2 and the stenotic tracheas were segmented with the ACM. Finally, the quantification of the stenosis was performed using the procedure described in Section 2.2.3. The results were reviewed by experts in the pulmonology field in order to evaluate the proposed method w.r.t. the estimated healthy trachea, the assessment of the stenosis, and the prediction of stents.

The ASM built for these experiments contained all the $N = 38$ healthy tracheas. All other parameters were set as in the simulation experiments.

3.3. Results

3.3.1. Point distribution model

In general, only the first t modes corresponding to a certain percentage of the total variance present in the PDM are used (Cootes et al., 1995). In fact, when all modes were used in the registration, the shape generated with the ASM became too flexible. As a result, it was more susceptible to the attraction caused by the regions with stenosis. The empirical choice of $t = 10$ modes in all experiments, which represented on average approximately 90% of the total variance captured by the model, eventually proved to be good enough.

Fig. 3 shows the first three modes of variation captured by the model, with the average shape in the middle and the shapes corresponding to $\pm 3\sqrt{\lambda_i}$ next to it. The mode with largest variation indicates changes in the calibre. The second mode represents global bending, and from then onwards different levels of local bending or twisting.

3.3.2. ASM registration

Fig. 4 shows how the *Fixed Landmarks* method acts on two examples, one extracted from the simulation experiments and the other from the experiments with clinical data. From left to right, the figure shows the image with the stenotic trachea, two
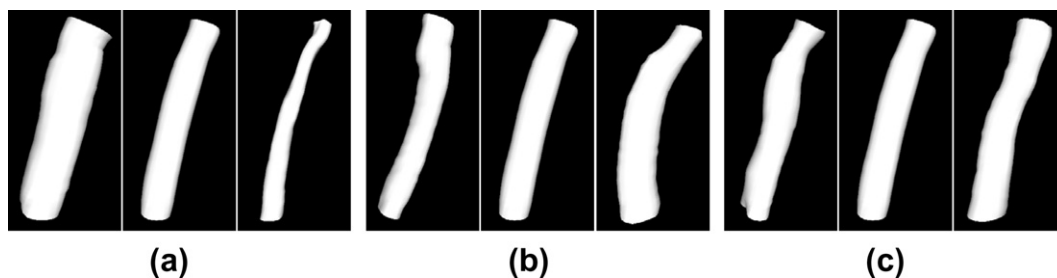

(a) **(b)** **(c)**

Fig. 3. From (a) to (c), the first three modes of variation. Each figure shows the average shape (middle), $-3\sqrt{\lambda_i}$ (left), and $+3\sqrt{\lambda_i}$ (right) along the mode.
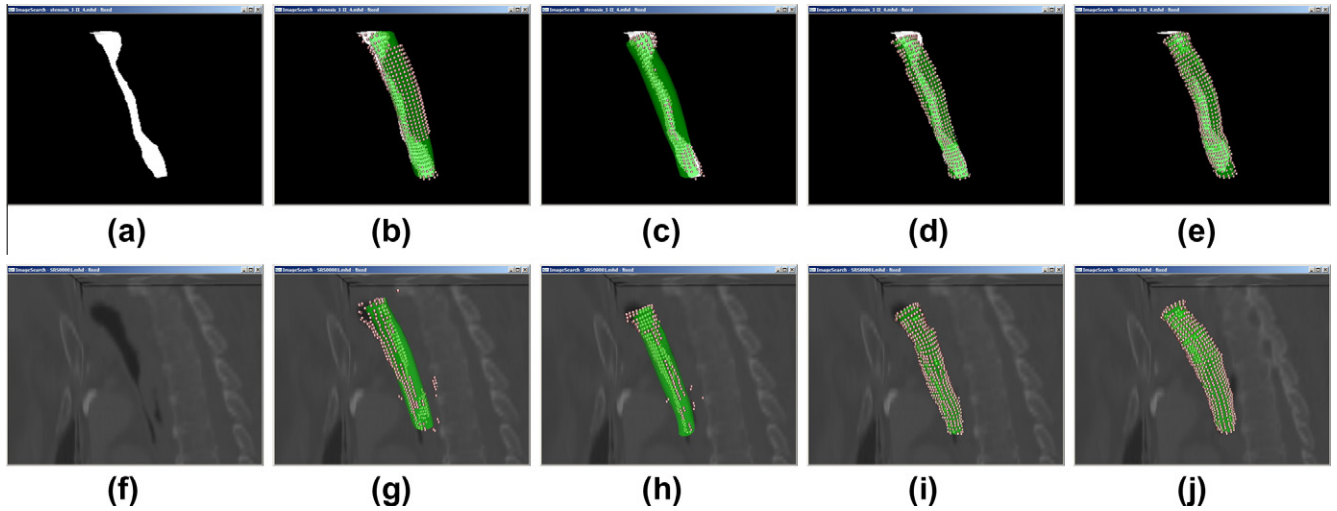
Fig. 4. Examples of the *Fixed Landmarks* method in action with simulation data (top) and clinical data (bottom). The green shape is the shape generated by the model at one iteration and the red dots indicate the landmarks of the candidate shape, which match high gradients in the image. From left to right, the figures show the trachea with stenosis, two non-consecutive steps of the rigid alignment and two non-consecutive steps of the *Fixed Landmarks*.

non-consecutive steps of the rigid alignment and two non-consecutive steps of the *Fixed Landmarks* method. The green shape indicates the shape $\hat{\mathbf{x}}^{(k)}$ and the red dots represent the landmarks of the candidate shape $\mathbf{y}^{(k+1)}$, as described in Section 2.1.4. Note that during the rigid alignment all the edges of the target trachea attract the landmarks, since the search profiles are long. This is necessary in order to find the correct position and orientation of the target. When the rigid alignment converges, the *Fixed Landmarks* immediately starts. Now, the landmarks for which $|d\mathbf{y}_{\mathbf{v}_j}^{(k+1)}| > d$ remain fixed w.r.t. $\hat{\mathbf{x}}^{(k)}$. Note that they remain far from the regions with stenosis. As the registration proceeds, the green shape takes the form of the target shape, guided by the healthy areas of the target and by the landmarks $\hat{\mathbf{x}}^{(k)}|_{\mathscr{L}''}$, which are those that remained fixed. Fig. 4e and j represent the final result, i.e., when the *Fixed Landmarks* converged.

3.3.3. Assessment of stenosis

Simulation data To quantify the error in the estimation of the healthy trachea, the following procedure was conducted. The phantoms generated from each originally healthy trachea were subdivided into $G = 10$ groups, according to the categories defined in Tables 1 and 2, each with a different size S_g. The reasoning behind this subdivision is to show how the *Fixed Landmarks* and the *TalwarWLS* behaved relative to variations in location, length, and degree of stenosis across the whole set of T leave-one-out tests. Let us then define, for a test instance t, $\delta_{\max_{gtp}}$ and $\delta_{\text{mean}_{gtp}}$ as the maximum and mean Hausdorff distances, respectively, between the estimated trachea for phantom p, of group g, and its original, healthy equivalent. These distances were obtained using the algorithm proposed in Aspert et al. (2002) and can be interpreted as the mean and maximum errors in the estimation of the healthy tracheas. Afterwards,

$$\bar{\delta}_{\max_{gt}} = \frac{1}{S_g} \sum_{p=1}^{S_g} \delta_{\max_{gtp}} \quad \text{and} \quad \bar{\delta}_{\text{mean}_{gt}} = \frac{1}{S_g} \sum_{p=1}^{S_g} \delta_{\text{mean}_{gtp}} \qquad (21)$$

were calculated as the average, per-group maximum and mean errors, respectively, for one test instance.

For the final comparison, each group's average maximum error, $\mu_{\max_g}$, and average mean error, μ_{mean_g}, were computed for each ASM registration method, across the whole set of T leave-one-out tests. That is,

$$\mu_{\max_g} = \frac{1}{T} \sum_{t=1}^{T} \bar{\delta}_{\max_g t} \quad \text{and} \quad \mu_{\text{mean}_g} = \frac{1}{T} \sum_{t=1}^{T} \bar{\delta}_{\text{mean}_g t}. \qquad (22)$$

Fig. 5a shows the values obtained for μ_{mean_g} and $\mu_{\max_g}$, respectively, along with their standard errors. Fig. 5b shows an example of the estimation of the healthy trachea for phantom 1.I-II-4P of the simulation data. The figures clearly indicate that the *Fixed Landmarks* was more accurate and more robust than the *TalwarWLS*. Note from Fig. 5a that the *Fixed Landmarks* not only yielded better results in general, but was also more resistant to variations in length and degree of stenosis.

Fig. 6 shows the results obtained from the experiments with simulation data for the assessment of stenosis. The graphs show area profiles of healthy and stenotic tracheas for both the estimation obtained with the ASM registration and the ground truth obtained with the originally healthy tracheas used to build the phantoms. Each row of Fig. 6 shows three categories of stenosis for a given trachea, located posteriorly, anteriorly, and symmetrically, respectively. The reader should note that in most cases the parameters of the stenosis were very close to the ground truth parameters. Yet, there were a few difficult situations.

In Fig. 6c, for instance, it was difficult to detect the start of the stenosis and the point of maximum degree. In the case of the start point, the reason for the error was that the calibre of the estimated trachea was slightly overestimated at the top, while in the point of maximum degree there was an underestimation of the calibre along the rest of the centre line. It is worth mentioning, however, that this is the most difficult simulation case, i.e., a long segment stenosis, in which few healthy areas are available in the target trachea to guide the registration of the ASM. Still, the method performed very well in other similar situations.

A different situation occurred in Fig. 6g. The absence of healthy posterior tracheal wall along the upper two thirds of the phantom misled the registration of the ASM, which eventually yielded an overestimation of the calibre of the trachea along its lower part. The result was that the estimated extension of the stenosis was much longer than the ground truth measurement, due to the faulty detection of the end point.

Fig. 7 presents statistics of the error of the estimated parameters of the stenoses relative to the ground truth for each of the $N' = 10$ tracheas used in the simulations. Note that the average error in degree between estimation and ground truth was around only 0.05 percentage points, while the error in the other parameters was
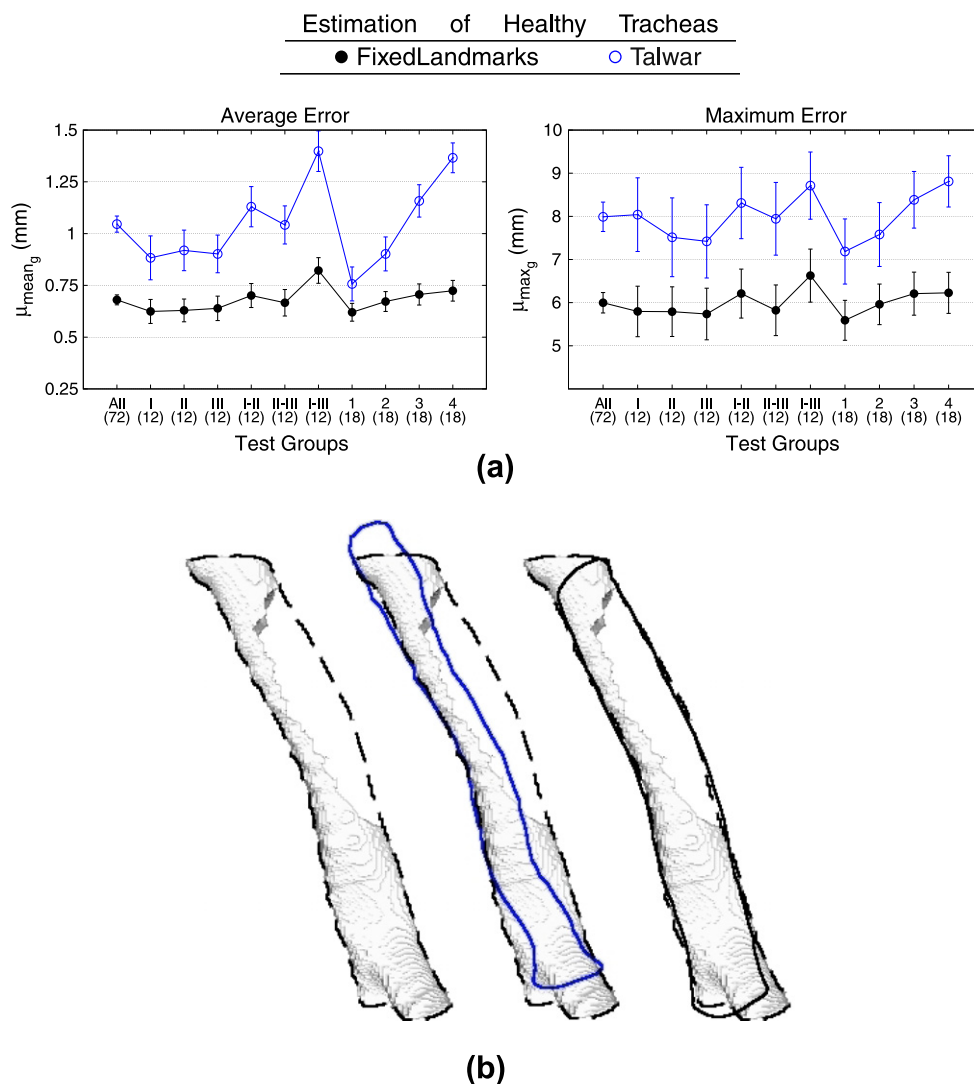
Fig. 5. (a) Quantified average and maximum errors, respectively, in the estimation of the healthy trachea when using the *Fixed Landmarks* and the *TalwarWLS* registration methods. The numbers in brackets indicate the number of phantoms, S_g, in each test group. (b) Example of the estimation of the healthy trachea for phantom 1.I-II-4P of the simulation data. From left to right, the phantom with the originally healthy trachea represented as a dashed line, estimation of the healthy trachea using *TalwarWLS* (blue line), and the estimation using *Fixed Landmarks* (solid black line). (For interpretation of the references to colour in this figure legend, the reader is referred to the web version of this article.)

around 5mm. At first, these results can be considered less than ideal. However, physicians can only choose between stents differing in length per centimetre, thus an average error of 5mm is in reality acceptable. Moreover, Fig. 7 reveals that the average and the standard deviation were severely affected by the presence of large outliers. In fact, most measurements within the 75 percentile were below the average, and the median of the errors in nearly all cases was less than 1.5mm.

The presence of outliers is explained by the large errors that can occur if the estimated healthy calibre is not adequate. The most difficult cases were those in which the stenosis had very low degree (a situation where stents are normally not employed) or extended through long segments. This can be evidenced in Fig. 8, which shows how the error varied per simulated category of stenosis. Indeed, categories 2 and I-III had the largest errors.

Fig. 9 shows the results obtained from the simulation experiments that used the *TalwarWLS* method instead of the *Fixed Landmarks*. The aim here is to confirm that the correctness in the assessment of the stenosis strongly depends on the quality of the estimation of the healthy trachea of the patient. Although the

results for the start and end points of the stenosis did not differ too much from those obtained with the *Fixed Landmarks*, the degree of narrowing, as expected, was considerably underestimated. The net result was that the errors in the assessment of the degree with respect to the ground truth were larger than when using the *Fixed Landmarks* method, as the figure demonstrates.

Clinical Data For the evaluation with clinical data, both objective and subjective evaluations were planned. For the objective evaluations, a special application was developed to allow the physicians to determine the parameters of stenosis based on the patient's CT image, in a way similar to what they do in their clinical practice. In this application, the physician visualizes the multiplanar reconstructions of the patients' CT scans and can navigate through the slices along each plane (see Fig. 10). Zooming and panning was provided in order to ease the visualization of the images. The objective was to manually select, with a simple mouse click, the points where the stenoses started, where they ended, where they reached their maximum degree, and to indicate the level of severity according to the values presented in Table 2.
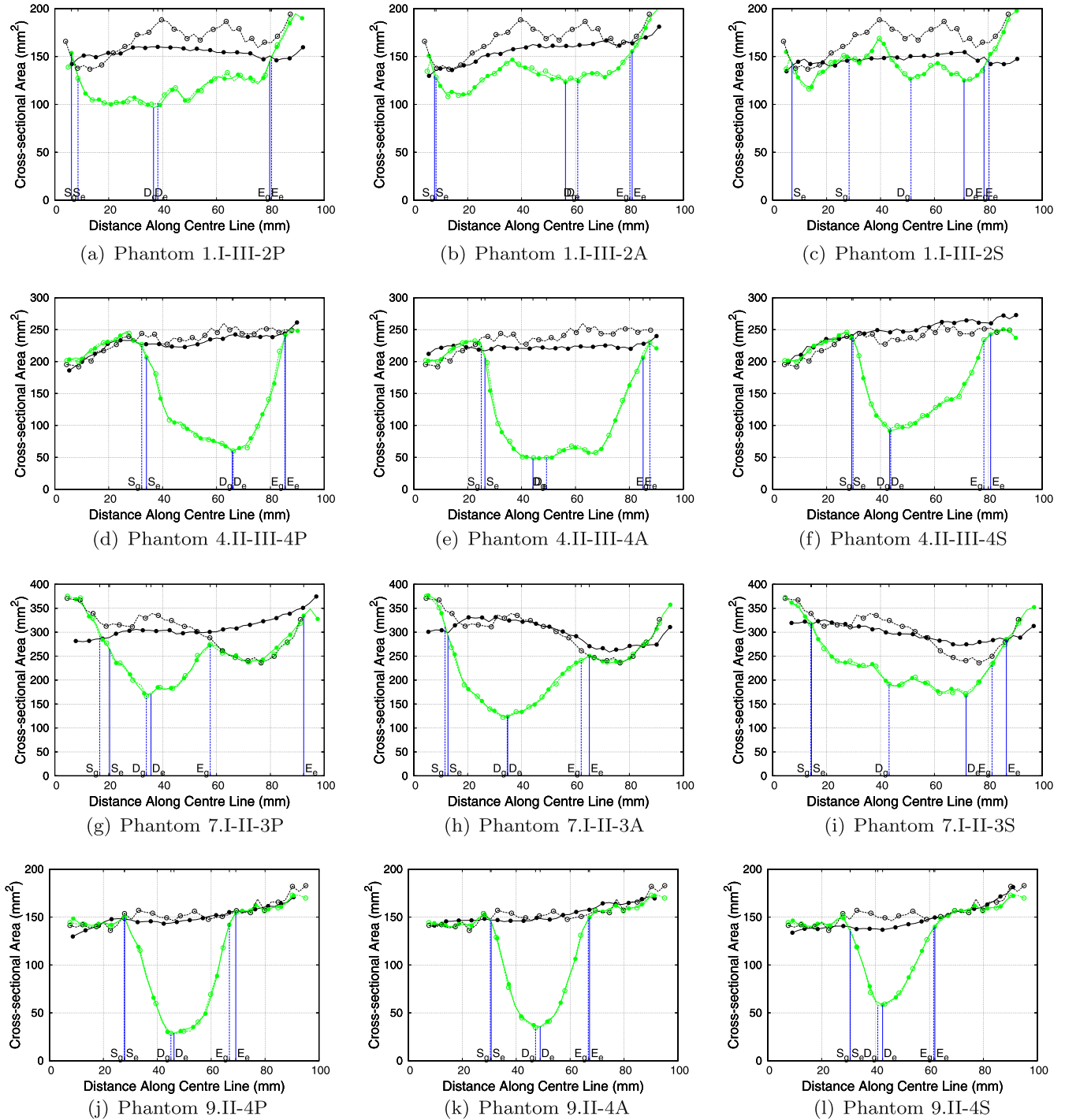
Fig. 6. Performance evaluation of the proposed stenosis detection procedure using simulated stenotic tracheas. For each position on the centre line (0 denotes the start of the trachea), the cross-sectional areas of the stenotic and healthy tracheas were obtained. Each row shows the results of three categories of stenosis, for a given trachea phantom, located posteriorly, anteriorly, and symmetrically (columns 1, 2, and 3, respectively). The vertical lines indicate the detected start (S), point of maximum degree (D), and end of the stenosis (E).

The purpose of creating the application above was to cross-check the results obtained with the proposed automatic assessment of stenosis and the results obtained from the experts' visual/manual assessments (the gold standard). The application was thus run by three experts in the pulmonology field and the results of their visual/manual assessments were recorded. Tables 3
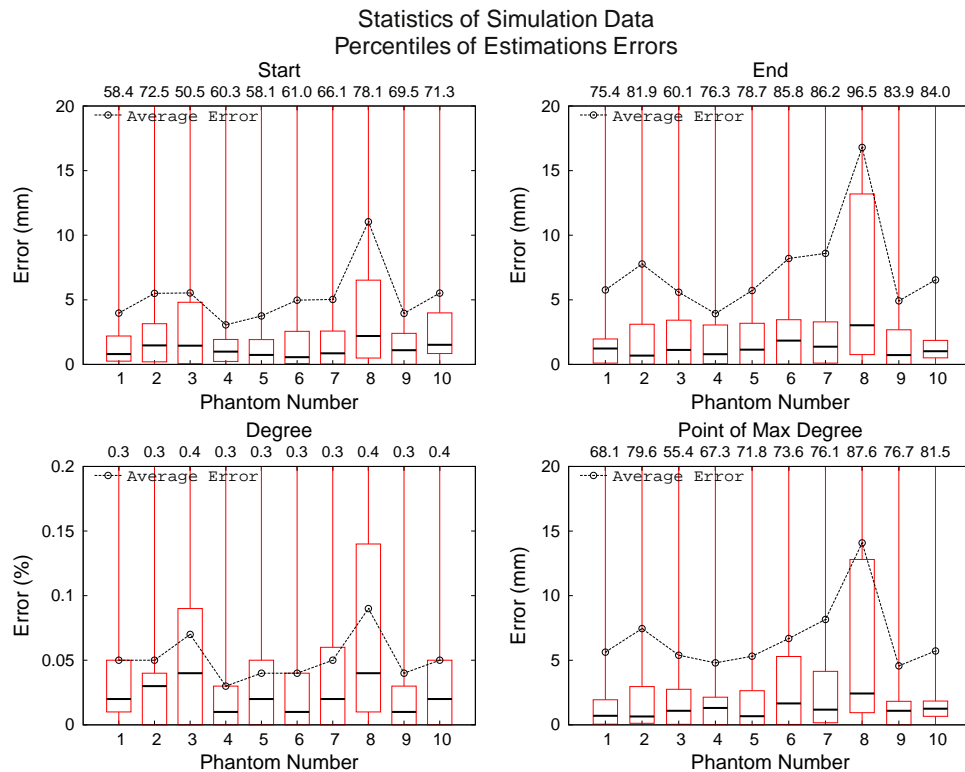
Fig. 7. The graphs show, for each phantom, the minimum, 1st quartile, median, 3rd quartile, maximum, and average errors of the estimated parameters of the 72 simulated categories of stenosis relative to the ground truth (the maximum values are shown at the top of the graph).
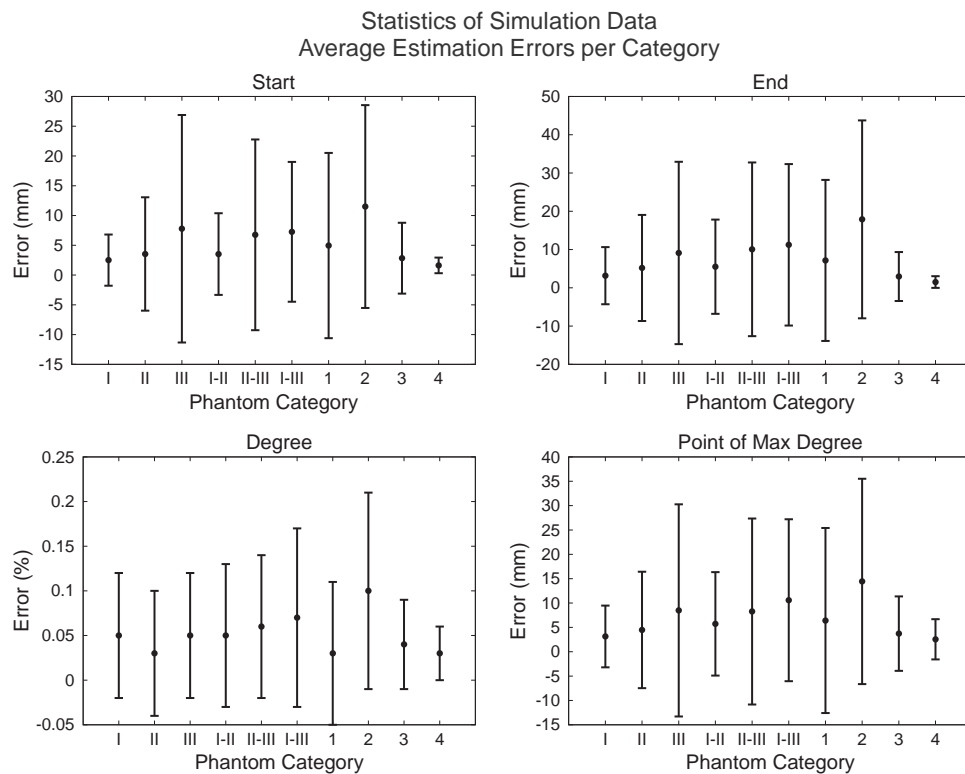

Fig. 8. Average estimation error per simulated category of stenosis, along with their respective standard deviations.

and 4 show a significant variability present in the recorded results for the stenoses of the 9 patients. With such variability, it is difficult to make an objective validation of the proposed automatic method against the manual evaluations. As a consequence, these data could not be used. Instead, they proved that stenosis assessment is indeed very operator dependent.
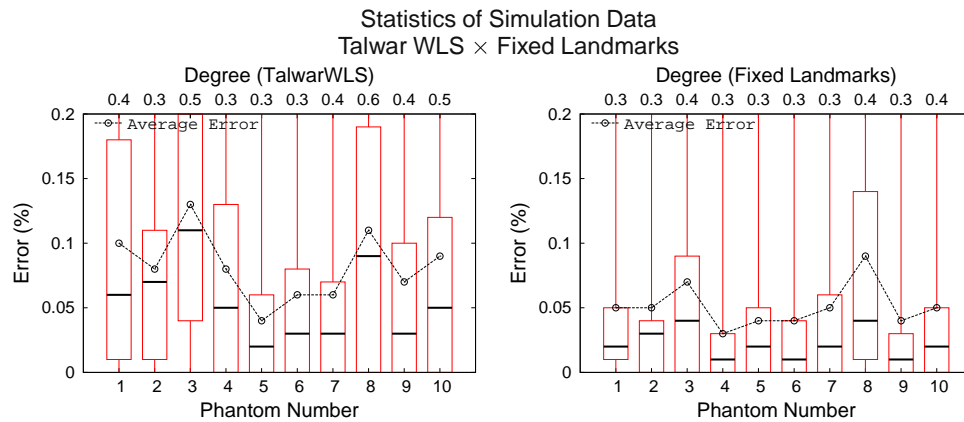
Fig. 9. The graphs show, for each phantom, the percentiles and average errors of the degree of narrowing of the 72 simulated categories of stenosis relative to the ground truth when using the *TalwarWLS* and the *Fixed Landmarks* methods.
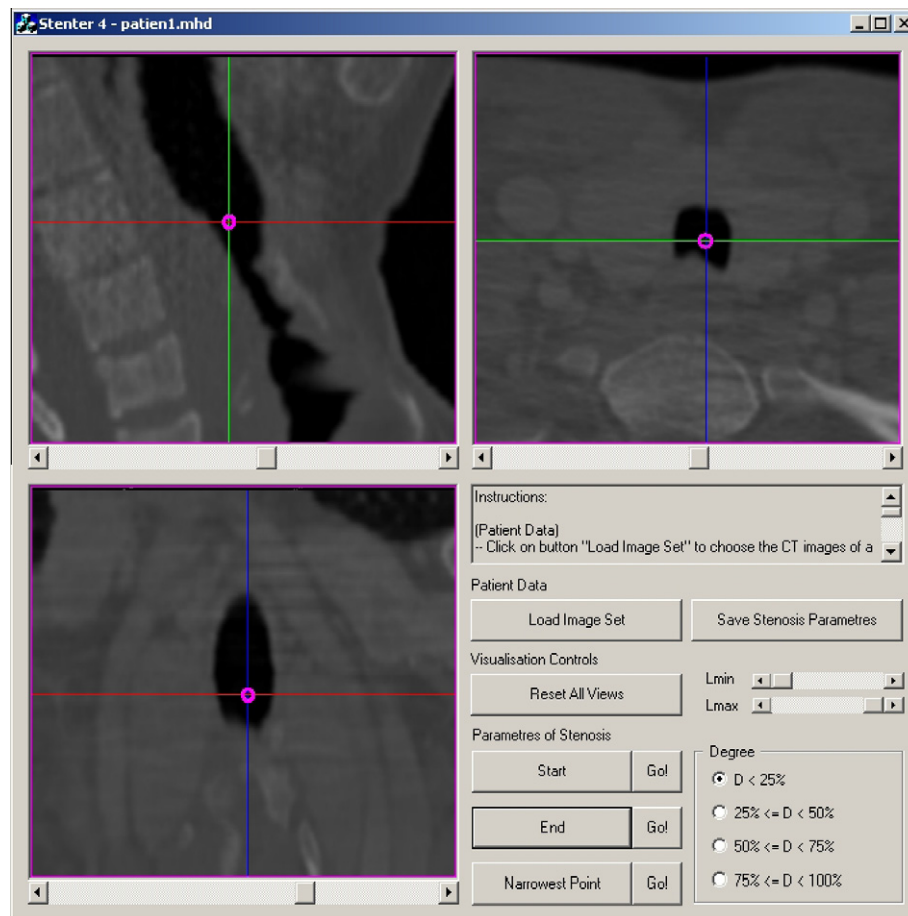

Fig. 10. GUI of the application developed for manual/visual assessment of stenosis. The expert marks on the patient's CT image the parameters of the stenosis (start, end, point of maximum degree) and chooses the degree of narrowing from ranges of values. Zooming and panning enhances the visualization.

Concerning the results obtained with the proposed method, healthy tracheas of plausible calibre and shape were yielded in nearly all cases, as can be seen in Fig. 11. In addition, the automatically detected parameters of the stenoses conformed to the diagnosed parameters, as described in Section 3.2. In the subjective evaluation, the consulted experts confirmed that the proposed automatic assessment of the stenosis and the suggested stents were accurate enough to support their diagnostic decisions. The proposed method therefore serves its purpose and sheds light in

the diagnostic process, by providing a common ground from which specialists can do their own assessment.

The good quality of the results does not mean, however, that difficult cases did not exist. The first difficult case was **Patient 3**, in Fig. 11c. The very unusual geometry of the patient's trachea hindered the registration of the ASM, which could not produce a plausible healthy shape along the narrowed areas. In the end, the stenosis, notably its degree, was largely underestimated. The second difficult case was **Patient 5**, shown in Fig. 11e. Since the

Table 3
Samples of the manual/visual measurements performed by three experts in the pulmonology field. All values are in millimetres and indicate the position along the axial axis where the corresponding parameters of the stenosis were marked by the experts, relative to the start of the patients' CT scan.

	Patient 1			Patient 3		
	Exp.1	Exp.2	Exp.3	Exp.1	Exp.2	Exp.3
Start	93.00	93.00	94.00	540.00	576.00	495.00
Pt. max degree	107.00	95.00	95.00	594.00	657.00	576.00
End	110	113	112	684.00	675.25	576.00
	Patient 6			Patient 7		
Start	151.00	170.00	145.00	55.00	64.00	73.00
Pt. max degree	189.00	185.00	174.00	87.00	81.00	86.00
End	198.00	194.25	187.00	99.00	96.00	91.00

stenosis had very low degree (even the official diagnostic mentioned only a suspicion that stenosis was present), the *Fixed Landmarks* did not succeed in differentiating between healthy and narrowed regions of the trachea. As a consequence, the narrowed regions had stronger influence on the registration of the ASM, and the method could not detect any narrowing at all.

3.3.4. Prediction of stents

Fig. 12 shows the predicted stents for some of the patients used in our experiments with clinical data. The stents are directly derived from the computed parameters of the stenosis, as described in Section 2.3. Note that they cover the stenosis according to the parameter R_0 defined at 0.8 (at least 20% of narrowing) and provide a plausible healthy calibre for the narrowed trachea. Nonetheless, an exception can be observed in **Patient 3**. As shown in Fig. 11c, the assessment of the stenosis in this case was faulty due to the highly deformed nature of the patient's trachea, which is evidenced in Fig. 12c.

4. Discussion

4.1. Fixed landmarks

Despite the good results obtained with the *Fixed Landmarks*, it is important to mention that the quality of the proposed method depends on the choice of the sets $\mathscr{L}'$ and $\mathscr{L}''$, which correspond to landmarks that are allowed to move and those that remain fixed at each iteration, respectively. These sets, in turn, depend on the choice of the threshold distance d. Intuitively, as d increases, the *Fixed Landmarks* tends to perform like the *StandardLS*, since $\mathscr{L}''$ will tend to be empty and no landmarks will remain fixed. The registration will thus not be guarded against the attraction of stenotic regions. Conversely, if d is too short, $\mathscr{L}'$ will tend to be empty and all landmarks will remain fixed. In the worst case, the latter situation will cause the resulting shape to be equal to the average shape of the ASM. Fig. 13 demonstrates this behaviour after the whole set

of simulation experiments were performed with different values of d. The graphs show how the error in the estimation of the degree of stenosis, the most sensitive parameter, varied with d.

One option to reduce the dependency on d is to let this parameter be set by the operator. Different values of d should then be tried until acceptable results are yielded. Another possibility is to devise an adaptive algorithm to change d as needed during the registration. For instance, d could be shortened as a function of the iteration number or could change according to the distribution of the landmark displacements. Nevertheless, the value $d = 1$ mm proved to be a good empirical choice in the hundreds of experiments performed with simulation and clinical data.

4.2. Issues when registering the ASM to tubular surfaces

As with any other open tubular surface, the registration of the ASM to tracheas may be hindered by two degrees of freedom. In the first, given that there may be no cues indicating the top and bottom limits of the trachea, the shape generated by the model may freely drift and eventually converge to unwanted locations. This can easily be circumvented by forcing limits to these displacements. Here, the limits are derived from the bounding box of the average shape of the ASM after the operator chooses its correct location and scale in order to initialize the registration. Setting the limits to 1 voxel above and below the bounding box is usually enough.

The second degree of freedom is related to rotation. A perfect tubular surface has no cues indicating correspondence w.r.t. the ASM registered to it. Consequently, the shape generated by the model may freely rotate around the target's centre line until convergence, possibly when the iteration limit is reached. In principle, some sort of restriction could be forced on rotations around the centre line of the trachea. However, a few cues are expected to be present in the case of the trachea, such as the carina. In addition, the operator can chose the initial orientation of the shape before the registration, as discussed earlier. Thus, no restrictions on rotations are set during the registration.

4.3. Segmentation of the stenotic trachea

One may argue that the segmentation of the stenotic trachea, as opposed to the approach adopted in this work, could be easily accomplished with, e.g., a 3D region growing method, as the one in Section 2.1.1, or a 2D slice based ACM to segment the tracheal lumen, as described in Triglia et al. (2002). However, such segmentation may be problematic if the stenosis is too severe, given little or no presence of tracheal lumen in the image, as also reported in Triglia et al. (2002). The proposed solution in that work was to manually reconstruct the missing parts of the trachea.

Patient 4 was an example of such a severely narrowed trachea among our experiments with clinical data. The lumen around the narrowed region was barely visible in the CT image and there was

Table 4
Variability in experts' manual/visual assessment of stenosis, for the nine patients used in the experiments. The table shows the standard deviation (in millimetres) observed when the experts manually determined the parameters of the stenoses.

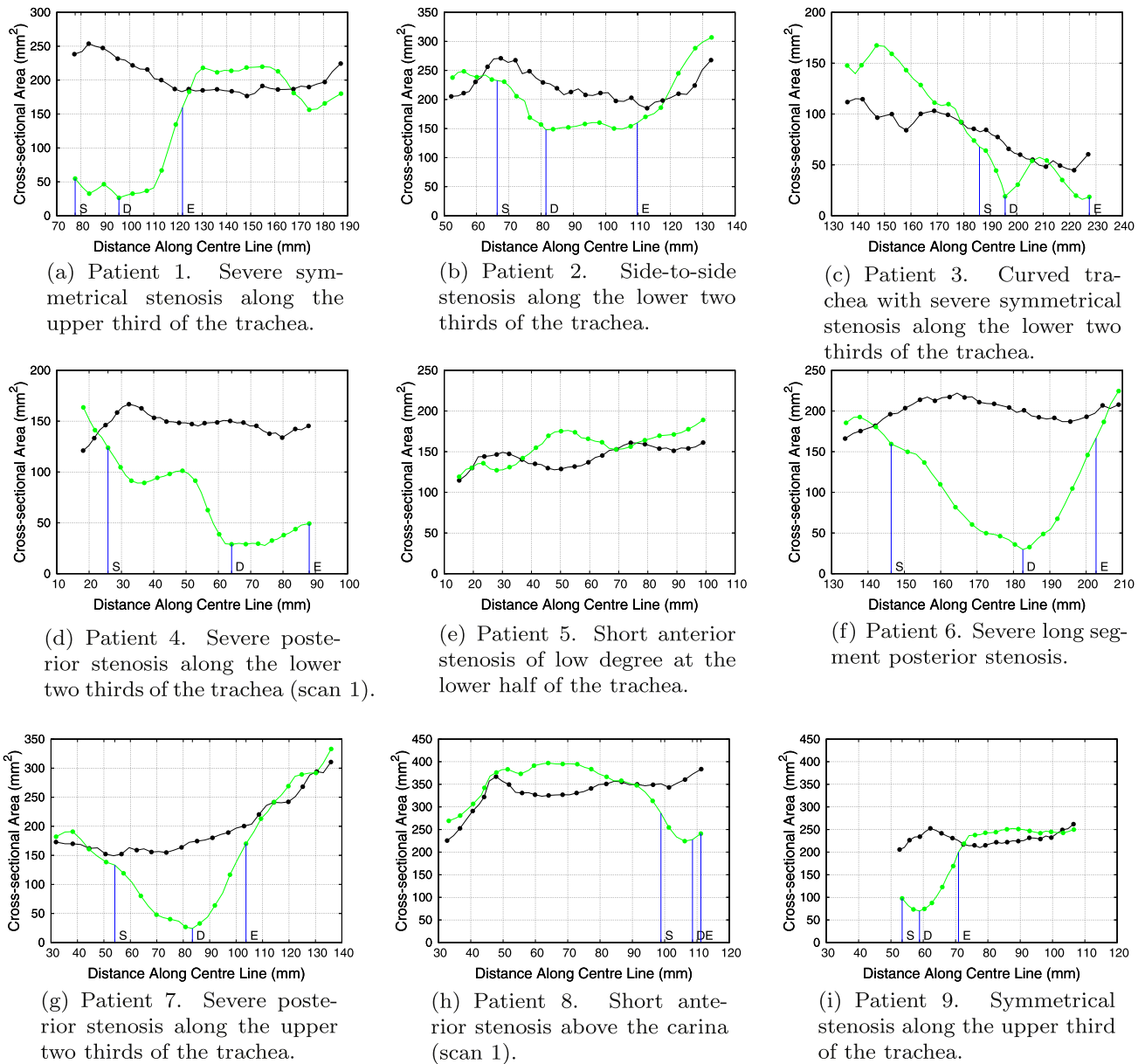|	P1	P2	P3	P4 (scan 1)	P4 (scan 2)	P5
Start	0.58	5.00	13.53	19.97	18.25	2.89
Pt. max degree	6.93	5.77	14.18	1.73	6.93	2.89
End	1.53	21.79	19.97	4.58	16.52	11.55
	P6	P7	P8 (scan 1)	P8 (scan 2)	P9	
Start	13.05	9.00	0.00	0.00	9.81	
Pt. max degree	7.77	3.21	0.00	0.00	3.46	
End	5.57	4.04	2.89	2.89	5.20	

Fig. 11. Examples of stenosis quantification for the experiments with clinical data. The vertical lines indicate the detected start, point of maximum degree, and end of the stenosis. The *x*-axis represents the distance along the centre line of the trachea, where 0 is the topmost position in the image.

only a hint of the tracheal wall. Fig. 14a shows the result of a simple 3D region growing applied to this CT scan. Note that a considerable part of the trachea is missing in the segmentation. The advantage of using the ACM to segment the trachea as proposed in this work is that it is able to reconstruct the tracheal wall for absent regions such as the one in this example, without manual intervention, thanks to the geometric constraints imposed by the internal forces of the model. The result of using the ACM is shown in Fig. 14b.

Nonetheless, it is worth mentioning that **Patient 4** was an especially difficult case. The problem here was that the oesophagus of

the patient was also visible in the image, exactly behind the narrowed region of the trachea. Since the initial shape for the ACM is the healthy estimation given by the ASM, the edges of the oesophagus in the image incurred a strong external force to the ACM. In fact, so strong that the ACM could only be successfully applied to this image after a pre-processing step to manually segment the trachea. The result of this pre-processing step was similar to that in Fig. 14a. After the pre-processing, the ACM was successfully applied to obtain the complete shape of the narrowed trachea, generating the result of Fig. 14b.
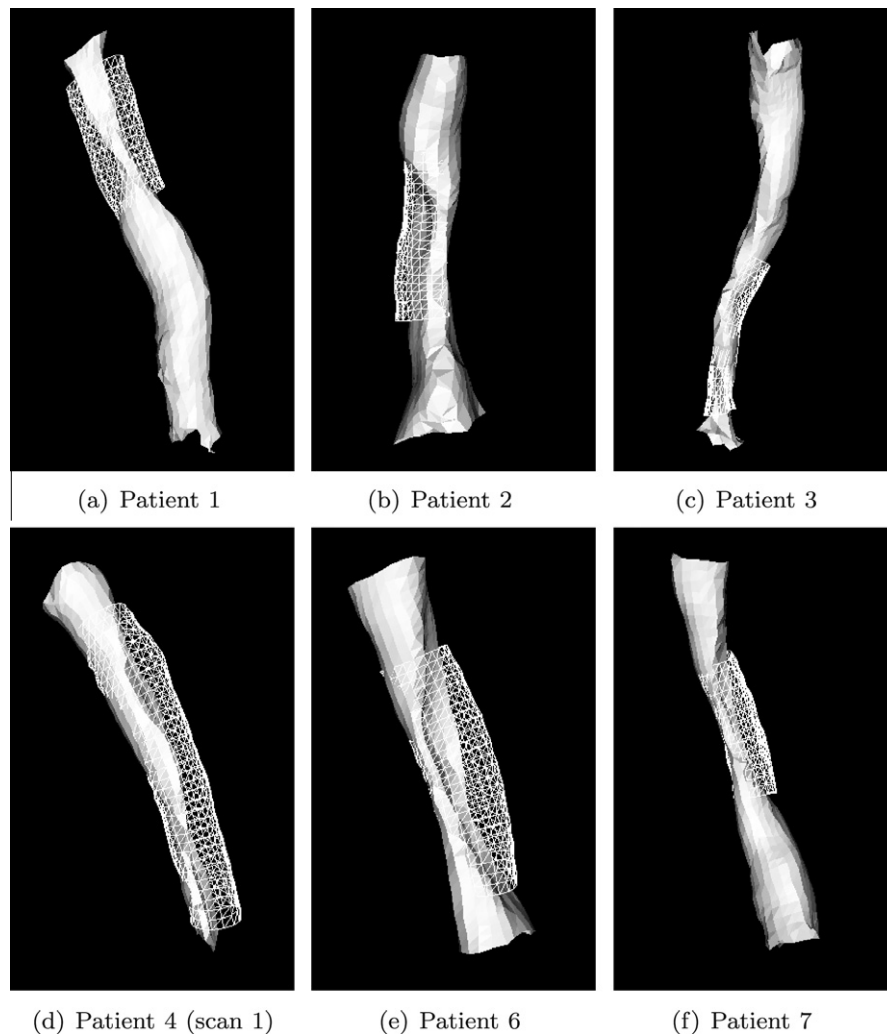
(a) Patient 1   (b) Patient 2   (c) Patient 3

(d) Patient 4 (scan 1)   (e) Patient 6   (f) Patient 7

Fig. 12. Visualization of the stents computed for the patients in the experiments with clinical data.

4.4. Execution times

Although a detailed time analysis was out of the scope of this work, a quick evaluation showed that each step of the overall method takes only a few seconds to run with the provided parameters. The machine used in the tests was an Intel® Core™ 2 Quad CPU, at 2.4 GHz, with 8 GB of RAM, running under Windows Vista™ Ultimate 64-bits, and all algorithms were implemented in C++. For one case, the measured times are given in Table 5. These results mean that the method is a viable tool to be used in the clinical setting.

4.5. Future work

A considerable step forward in the proposed framework would be to extend the stent prediction with a functional analysis of airways through airflow simulations. By doing this, other parameters such as the type of the stent and even the thickness of the airway wall (which may co-determine the responsiveness of the trachea to the stent) could be added to the model. A numerical model of the tracheal deformation could take into account the responsiveness of the trachea to the predicted stent. All these results could be fed back into the stent prediction so that the choice of stent could be optimized.

Although the focus of the present work was on tracheal stenosis, it is reasonable to expect that the *Fixed Landmarks* method could also be applied on vascular stenoses. The difficulties in this case would mostly lie in the fact that arteries have a much larger global shape variability than tracheas and that longitudinal versus radial scale is also much larger in arteries. As a consequence, it could be difficult to build an ASM of healthy arteries that would be completely resistant to the regions where the stenoses occur. Still, arteries can usually be efficiently segmented with the use of contrast agents, which could at least remove the interference of noise and the presence of neighbouring structures.

There are also reasons to believe that the *Fixed Landmarks* method could be used as a *Robust ASM Fitting* approach in general. Since ASM registrations yield only objects that resemble those in the training set, keeping landmarks fixed with respect to their position in the previous iteration of the registration immediately removes the influence of outliers among the residuals. The fixed landmarks, together with those that were allowed to move, eventually help the registration generating the desired shape.
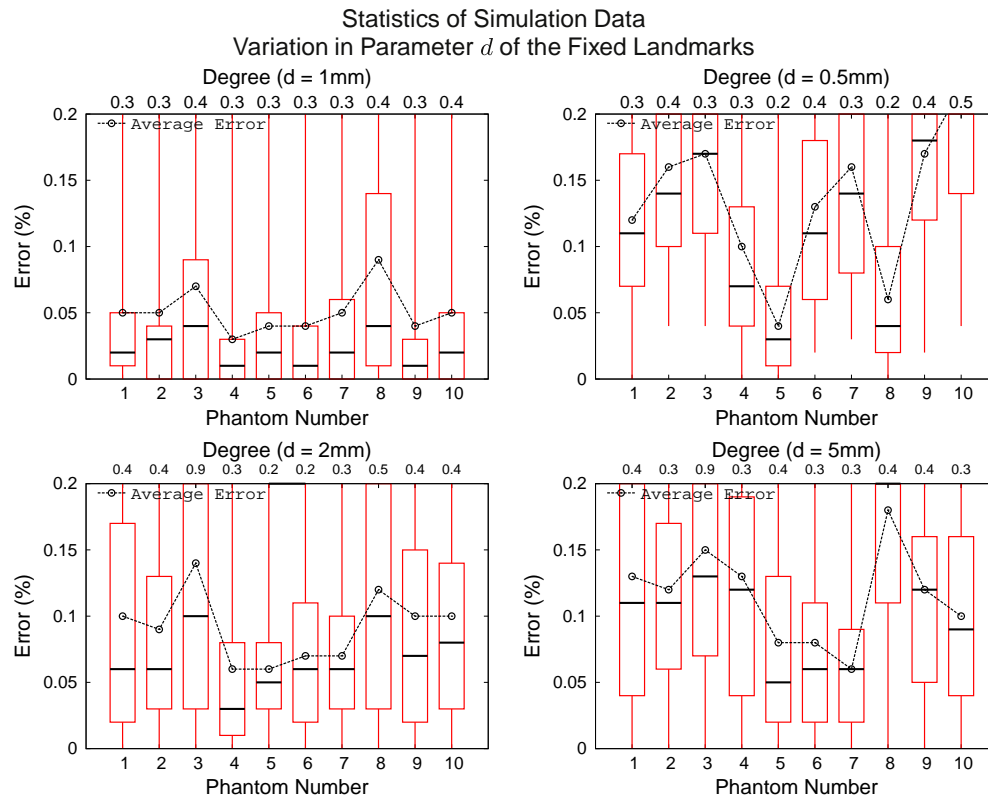
Fig. 13. Variation in the results obtained from the simulation experiments when varying the parameter *d* of the *Fixed Landmarks* method. The graphs show how the error in the computation of the degree of narrowing of the stenosis increased when $d \neq 1$ mm.
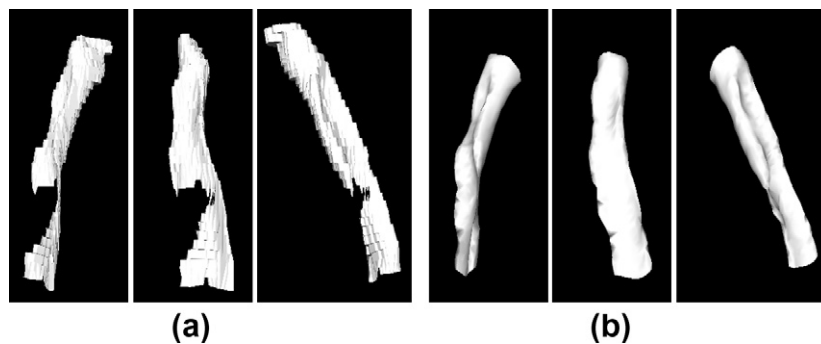

Fig. 14. Illustration of a difficult case (**Patient 4**) due to severe stenosis (a) and how the ACM managed to reconstruct the missing part of the tracheal wall (b).

Table 5
Approximate execution times of each step of the proposed method, measured for one example case.

Execution times		
ASM	ACM	Stenosis + stents
~30 s	~60 s	~1 s

5. Conclusion

Tracheal stents have widely been used in the treatment of tracheal stenosis. Choosing the correct length and diameter of the stent according to the patient, however, is an important preoperative step. Current stent estimation methods cannot trivially predict the diameter of the desired healthy trachea over the stenotic region and are very operator dependent. The present work proposed a method that estimates the healthy trachea of a patient, as if stenosis was not present, using an active shape model (ASM) of healthy tracheas. The resulting shape matches the walls of the narrowed trachea except in areas where stenosis exists. This shape is used as input to an active contour model (ACM) that segments the narrowed trachea from the CT image of the patient. The ratio between the cross-sectional area profiles of healthy and narrowed tracheas eventually determines the start, end, and the degree of stenosis. This enables the calculation of the healthy tracheal calibre and of the length of the stenotic region, parameters used in the estimation of stents.

The proposed method was shown to be valuable as a decision support system to assist the preoperative planning of tracheal stent implants and the treatment of tracheal stenosis in general. With little human intervention, this method does not suffer from inter and intra-subject variations present in previous procedures.

Moreover, each step of the overall process does not take more than a few seconds to complete, making it a viable tool for the clinical setting.

References

Aspert, N., Santa-Cruz, D., Ebrahimi, T., 2002. Mesh: measuring errors between surfaces using the hausdorff distance. In: Proceedings of the IEEE International Conference on Multimedia and Expo, vol. I, pp. 705–708.

Ballester, M.A.G., del Palomar, A.P., Villalobos, J.L.L., Rodríguez, L.L., Trabelsi, O., Pérez, F., Ginel Cañamaque, Ángel, Cortés, E.B., Panadero, F.R., Castellano, M.D., Jover, J.H., 2009. Surgical planning and patient-specific biomechanical simulation for tracheal endoprostheses interventions. In: Medical Image Computing and Computer-Assisted Intervention – MICCAI 2009. Lecture Notes in Computer Science, vol. 5762. Springer, pp. 275–282.

Behiels, G., Maes, F., Vandermeulen, D., Suetens, P., 2002. Evaluation of image features and search strategies for segmentation of bone structures in radiographs using active shape models. Medical Image Analysis 6 (1), 47–62.

Boiselle, P.M., Catena, J., Ernst, A., Lynch, D.A., 2008. Tracheobronchial stenoses. In: CT of the Airways. Humana Press – Springer, pp. 121–149.

Borgefors, G., 1986. Distance transformations in digital images. Computer Vision Graphics and Image Processing 34 (3), 344–371.

Carretta, A., Melloni, G., Ciriaco, P., Libretti, L., Casiraghi, M., Bandiera, A., Zannini, P., 2006. Preoperative assessment in patients with postintubation tracheal stenosis. Surgical Endoscopy 20 (6), 905–908.

Ching-Yang, W., Yun-Hen, L., Ming-Ju, H., Yi-Chen, W., Ming-Shian, L., Po-Jen, K., Hui-Ping, L., 2007. Airway stents in management of tracheal stenosis: have we improved? ANZ Journal of Surgery 77, 27–32. 6.

Cohen, L., Cohen, I., 1993. Finite-element methods for active contour models and balloons for 2-d and 3-d images. IEEE Transactions on Pattern Analysis and Machine Intelligence 15 (11), 1131–1147.

Cootes, T.F., Taylor, C.J., Cooper, D.H., Graham, J., 1995. Active shape models: their training and application. Computer Vision and Image Understanding 61 (1), 38–59.

de Bruijne, M., van Ginneken, B., Niessen, W.J., Loog, M., Viergever, M.A., February 2003. Model-based segmentation of abdominal aortic aneurysms in cta images. In: Proceedings of SPIE Medical Imaging, vol. 5032. San Diego, CA, USA, pp. 1560–1571.

de Bruijne, M., Lund, M.T., Tank=, L.B., Pettersen, P.C., Nielsen, M., 2007. Quantitative vertebral morphometry using neighbor-conditional shape models. Medical Image Analysis 11 (5), 503–512.

Elliott, M., Roebuck, D., Noctor, C., McLaren, C., Hartley, B., Mok, Q., Dunne, C., Pigott, N., Patel, C., Patel, A., Wallis, C., 2003. The management of congenital tracheal stenosis. International Congress Series 1254, 321–334. advances in Pediatric ORL. Proceedings of the 8th International Congress of Pediatric Otorhinolaryngology.

Freitag, L., Ernst, A., Unger, M., Kovitz, K., Marquette, C., 2007. A proposed classification system of central airway stenosis. European Respiratory Journal (30), 7–12.

Graham, S.M., McLennan, G., Funk, G.F., Hoffman, H.T., McCulloch, T.M., Cook-Granroth, J., Hoffman, E.A., 2000. Preoperative assessment of obstruction with computed tomography image analysis. American Journal of Otolaryngology 21 (4), 263–270.

Grillo, H.C., Donahue, D.M., Mathisen, D.J., Wain, J.C., Wright, C.D., 1995. Postintubation tracheal stenosis: treatment and results. The Journal of Thoracic and Cardiovascular Surgery 109 (3), 486–493.

Hoppe, H., Dinkel, H.-P., Walder, B., von Allmen, G., Gugger, M., Vock, P., 2004. Grading airway stenosis down to the segmental level using virtual bronchoscopy. Chest 125 (2), 704–711.

Kass, M., Witkin, A., Terzopoulos, D., 1988. Snakes: active contour models. International Journal of Computer Vision V1 (4), 321–331.

Kiesler, K., Gugatschka, M., Sorantin, E., Friedrich, G., 2007. Laryngo-tracheal profile: a new method for assessing laryngo-tracheal stenoses. European Archives of Oto-Rhino-Laryngology 264 (3), 251–256.

Lee, K.S., Lunn, W., Feller-Kopman, D., Ernst, A., Hatabu, H., Boiselle, P.M., 2005. Multislice CT evaluation of airway stents. Journal of Thoracic Imaging 20 (2), 81–88.

Mandour, M., Remacle, M., de Heyning, P.V., Elwany, S., Tantawy, A., Gaafar, A., 2003. Chronic subglottic and tracheal stenosis: endoscopic management vs.surgical reconstruction. European Archives of Oto-Rhino-Laryngology 260 (7), 374–380.

Miyazawa, T., Miyazu, Y., Iwamoto, Y., Ishida, A., Kanoh, K., Sumiyoshi, H., Doi, M., Kurimoto, N., 2004. Stenting at the flow-limiting segment in tracheobronchial stenosis due to lung cancer. American Journal of Respiratory and Critical Care Medicine 169 (10), 1096–1102.

Nouraei, S.A.R., McPartlin, D.W., Nouraei, S.M., Patel, A., Ferguson, C., Howard, D.J., Sandhu, G.S., 2006. Objective sizing of upper airway stenosis: a quantitative endoscopic approach. The Laryngoscope 116 (1), 12–17.

Pinho, R., Luyckx, S., Sijbers, J., September 2009a. Robust region growing based intrathoracic airway tree segmentation. In: 2nd International Workshop on Pulmonary Image Analysis. London, England, pp. 261–271.

Pinho, R., Tournoy, K., Gosselin, R., Sijbers, J., September 2009b. Assessment of tracheal stenosis using active shape models of healthy tracheas: a surface registration study. In: 2nd International Workshop on Pulmonary Image Analysis. London, England, pp. 125–136.

Prasad, M., Bent, J.P., Ward, R.F., April, M.M., 2002. Endoscopically placed nitinol stents for pediatric tracheal obstruction. International Journal of Pediatric Otorhinolaryngology 66 (2), 155–160.

Rajamani, K.T., Styner, M.A., Talib, H., Zheng, G., Nolte, L.P., Ballester, M.A.G., 2007. Statistical deformable bone models for robust 3d surface extrapolation from sparse data. Medical Image Analysis 11 (2), 99–109.

Rogers, M., Graham, J., 2002. Robust active shape model search. In: Proceedings of the 7th European Conference on Computer Vision-Part IV. Springer-Verlag, pp. 517–530.

Saito, Y., Imamura, H., 2005. Airway stenting. Surgery Today 35 (4), 265–270.

Shitrit, D., Valdsislav, P., Grubstein, A., Bendayan, D., Cohen, M., Kramer, M., 2005. Accuracy of virtual bronchoscopy for grading tracheobronchial stenosis: correlation with pulmonary function test and fiberoptic bronchoscopy. Chest 128 (5), 3545–3550.

Sorantin, E., Halmai, C., Erdhelyi, B., Palgyi, K., Nyl, L., OllT, L.K., Geiger, B., Lindbichler, F., Friedrich, G., Kiesler, K., 2002. Spiral-CT-based assessment of tracheal stenoses using 3-D-skeletonization. IEEE Transactions on Medical Imaging 21 (3), 263–273.

Spittle, N., McCluskey, A., 2000. Lesson of the week: tracheal stenosis after intubation. British Medical Journal 321 (7267), 1000–1002.

Stamenkovic, S., Hierner, R., De Leyn, P., Delaere, P., 2007. Long-segment tracheal stenosis treated with vascularized mucosa and short-term stenting. Annals of Thoracic Surgery 83 (3), 1213–1215.

Theobald, B.-J., Matthews, I., Baker, S., April 2006. Evaluating error functions for robust active appearance models. In: Proceedings of the International Conference on Automatic Face and Gesture Recognition, pp. 149–154.

Triglia, J.-M., Marciano, S., Nazarian, B., Moulin, G., Sudre-Levillain, I., Giovanni, A., 2002. Virtual laryngotracheal endoscopy based on geometric surface modeling using spiral computed tomography data. The Annals of Otology, Rhinology & Laryngology 111 (1), 36–43.

Valdes, R., Yanez-Suarez, O., Medina, V., 2000. Trachea segmentation in CT images using active contours. In: Proceedings of the 22nd Annual International Conference of the IEEE Engineering in Medicine and Biology Society, 2000, vol. 4, pp. 3184–3187.

Venuta, F., Rendina, E.A., de Giacomo, T., November 2004. Airway stenting. <http://www.ctsnet.org/sections/clinicalresources/thoracic/expert_tech-1.html>.

Zachow, S., Lamecker, H., Elsholtz, B., Stiller, M., 2005. Reconstruction of mandibular dysplasia using a statistical 3d shape model. Proceedings of Computer Assisted Radiology and Surgery, vol. 1281. Elsevier, pp. 1238–1243.